This article has been accepted for inclusion in a future issue of this journal. Content is final as presented, with the exception of pagination.

Wave Simulation in Partially Saturated Porothermoelastic Media

Enjiang Wang, José M. Carcione, and Jing Ba

***Abstract*— In wave propagation in rocks, the strain field affects the internal energy such that compressed regions become hotter and expanded regions cooler. This thermoelastic effect is that the lack of thermal equilibrium between various parts of the vibrating medium and energy is dissipated when irreversible heat flow driven by the temperature gradient occurs. Moreover, rocks are generally partially saturated and the interfacial tension between fluids affects the acoustic properties and induces additional slow P waves. To model these phenomena, we develop a generalized porothermoelasticity theory, including the Lord–Shulman (LS) and Green–Lindsay (GL) theories, for wave propagation in partially saturated nonisothermal media. The dynamical equations have as solutions the classical P1 and S waves and three slow waves modes, namely, the slow P2, slow P3, and the thermal (T) waves, which present diffusive behavior depending on the viscosity, frequency, and thermal properties. We compute the wavefields with a direct meshing algorithm by using an optimized finite-difference (FD) method to obtain the spatial derivatives and a first-order explicit Crank–Nicolson method for temporal extrapolation. The simulated snapshots and waveforms for the homogeneous and heterogeneous models with two different sets of thermal properties illustrate the characteristics of propagation as a function of frequency and saturation, which are consistent with the plane-wave analyses. The GL model can predict a higher thermal attenuation of the P1 wave and, consequently, a larger velocity dispersion than the LS theory. The thermal relaxation peak moves to low frequencies as the conductivity increases. This study is relevant to understand wave propagation in porous rocks and high temperature and pressure fields.**

***Index Terms*— Attenuation, dispersion, partially saturation, plane-wave analysis, porothermoelasticity theory, wave simulation.**

I. Introduction

WAVE propagation in fluid-saturated nonisothermal media is affected by the porous nature of rocks and their thermal properties [1], [2]. The theory of porothermoelasticity (or thermoporoelasticity) couples the fields of elastic deformation with temperature, combining the poroelasticity and heat equations, being relevant in a variety of fields, such as thermodynamics, chemical engineering, geothermal exploration, and earthquake seismology [3]–[6].

The theory of poroelasticity has been established by Biot [1], [7]. He considered the medium as a matrix (skeleton or frame) fully saturated with a fluid and derived the fundamental constitutive relations based on the Lagrange equations and the Hamilton principle. The theory predicts two compressional (P) waves and one shear wave. The second P wave is diffusive at low frequencies and wavelike with a low velocity at high frequencies. Many numerical techniques have been developed to simulate wave propagation in Biot-type media, including finite difference (FD) [8], [9] and discontinuous Galerkin [10], [11]. Biot applied continuum mechanics to macroscopic quantities. Many generalizations of the Biot theory have been proposed, including two fluids [12], [13], two solids [14]–[16], and double-porosity theories [17], [18]. Santos *et al.* [12] considered a frame saturated by a mixture of two immiscible fluids and derived dynamical equations based on the principle of virtual complementary work and Lagrangian variational theory. The model predicts an additional highly attenuated compressional wave, due to interfacial tension between the fluids (capillary pressure). Later, Lo *et al.* [13] proposed a similar theory. To model waves in heterogeneous poroelastic media, Santos *et al.* [19] developed finite-element solutions for simulating wave propagation. Carcione *et al.* [20] performed simulations by using the Fourier method and a time-splitting scheme combined with a Runge–Kutta time stepping.

Thermoelastic attenuation, due to the conversion of the fast P wave to the thermal (T) wave, is analogous to poroelastic attenuation [21]. Biot [2] derived parabolic-type thermal differential equations based on the classical heat conduction theory, but the formulation has unphysical solutions such as discontinuities and infinite velocities as a function of frequency. To overcome this problem, Lord and Shulman [22] adopted a hyperbolic-type heat equation with a relaxation time. The theory predicts a wavelike propagation with finite velocities at high frequencies. Green and Lindsay [23] proposed a similar generalization by introducing another relaxation time into the constitutive relations. Rudgers [24] obtained the plane-wave solutions and showed the existence of two P waves and an S wave. The second P wave is diffusive at low frequencies and wavelike at high frequencies, whose behavior is similar to that of the slow P wave of poroelasticity. More recently,

Manuscript received September 23, 2020; revised December 9, 2020; accepted December 14, 2020. This work was supported in part by the National Nature Science Foundation of China under Grant 41804095 and in part by the China Postdoctoral Science Foundation under Grant 2020M682242. *(Corresponding author: Jing Ba.)*

Enjiang Wang is with the Key Laboratory of Submarine Geosciences and Prospecting Techniques, Ministry of Education, College of Marine Geosciences, Ocean University of China, Qingdao 266100, China, and also with the Evaluation and Detection Technology Laboratory of Marine Mineral Resources, Qingdao National Laboratory for Marine Science and Technology, Qingdao 266061, China.

José M. Carcione is with the National Institute of Oceanography and Applied Geophysics (OGS), 34010 Trieste, Italy, and also with School of Earth Sciences and Engineering, Hohai University, Nanjing 211100, China.

Jing Ba is with the School of Earth Sciences and Engineering, Hohai University, Nanjing 211100, China (e-mail: jba@hhu.edu.cn).

Color versions of one or more figures in this article are available at https://doi.org/10.1109/TGRS.2020.3045515.

Digital Object Identifier 10.1109/TGRS.2020.3045515

using the theory of Lord–Shulman (LS), Carcione *et al.* [25] solved the wave propagation problem with a direct grid method based on the Fourier pseudospectral operator and an explicit Crank–Nicolson time-integration method.

The theory of porothermoelasticity couples the stress components with the temperature field in fluid-saturated porous media [5], [26]. Sharma [5] considered a thermally conducting isotropic porous solid saturated with a single fluid and proposed a theory combining the Biot poroelasticity and LS theories. The dynamical equations predict four waves, namely, a fast P wave, a slow Biot wave, a slow T wave, and the S wave. The two slow waves present a diffusive behavior under certain conditions, depending on the viscosity, frequency, and thermoelasticity constants, whereas the S wave is not affected by the thermal property.

On the other hand, immiscible fluids exist in porous media such as natural reservoirs, particularly in low-permeability tight rocks, and account for wave anelasticity in the presence of capillary pressure [27]. Zhou *et al.* [28] formulated a set of equations for wave propagation in unsaturated porothermoelastic media composed of a frame and pores filled with liquid and gas. They adopted a generalized non-Fourier heat conduction law involving two relaxation times, which leads to the implicit extrapolations of the temperature field during the computation. They do not explicitly mention the interfacial tension between fluids, as in the theory of Santos *et al.* [12], but the fact is that the fluids have different pressures, and it means that the concept of capillary pressure is implicitly incorporated. The equations similarly describe thermal attenuation as the LS theory. This theory predicts four P waves, namely, a fast P wave, a slow T wave, a fluid-related slow wave, and a gas-related slow wave. The former three waves are similar to those of porothermoelasticity. The additional gas-related slow wave has a very low velocity.

In the present work, we develop a modeling algorithm to simulate wave propagation in the heterogeneous partially saturated porothermoelastic media. We propose a generalization of the constitutive relations of Zhou *et al.* [28] to account for attenuation based on the LS and Green–Lindsay (GL) theories, involving a set of relaxation times. The velocity–stress–temperature formulation in the nonuniform porosity case is then derived and the corresponding plane-wave solutions are obtained, with which the propagation characteristics (velocity and attenuation) as a function of frequency are analyzed. We solve the equations numerically by using a direct grid method (i.e., mesh-based) based on an FD method to compute the spatial derivatives [29] and a Crank–Nicolson time-integration method. Numerical examples are carried out and conclusions are drawn accordingly.

II. Basic Theory

The partially saturated porothermoelasticity theory is established with the mass balance equations, generalized Darcy law, momentum balance equations, and generalized non-Fourier heat conduction law of the three-phase medium composed of grains (s), saturated with a liquid (l) and a gas (g). The saturations S^l and S^g measure the volume fractions occupied by the liquid and gas, respectively, and are related by $S^l + S^g = 1$.

Consider a 2-D isotropic medium and define v_i, $w_i^{(l)}$ and $w_i^{(g)}$, $i = x, z$, are the components of the particle velocity fields of the frame, and liquid and gas relative to the solid, respectively, σ_{ij} is the components of the total stress tensor, p_l and p_g are the liquid and gas pressures, and T is the increment of temperature above a reference absolute temperature T_0. Following Zhou *et al.* [28], the constitutive equations in partially saturated porothermoelastic media are

$$\begin{cases} \dot{\sigma}_{xx} = 2\mu v_{x,x} + \lambda\epsilon_m - \alpha\dot{p} - \beta_s[\dot{T} + (1-\epsilon)\tau_1\ddot{T}] + f_{xx} \\ \dot{\sigma}_{zz} = 2\mu v_{z,z} + \lambda\epsilon_m - \alpha\dot{p} - \beta_s[\dot{T} + (1-\epsilon)\tau_1\ddot{T}] + f_{zz} \\ \dot{\sigma}_{xz} = \mu(v_{x,z} + v_{z,x}) + f_{xz} \\ p = \gamma p_l + (1-\gamma)p_g \\ -\dot{p}_l = a_{11}\epsilon_m + a_{12}\epsilon_l + a_{13}\epsilon_g + a_{14}[\dot{T} + (1-\epsilon)\tau_1\ddot{T}] + f_l \\ -\dot{p}_g = a_{21}\epsilon_m + a_{22}\epsilon_l + a_{23}\epsilon_g + a_{24}[\dot{T} + (1-\epsilon)\tau_1\ddot{T}] + f_g \\ \epsilon_m = v_{x,x} + v_{z,z}, \; \epsilon_l = w_{x,x}^{(l)} + w_{z,z}^{(l)}, \; \epsilon_g = w_{x,x}^{(g)} + w_{z,z}^{(g)} \end{cases} \tag{1}$$

where, f_{xx}, f_{zz}, f_{xz}, f_l, and f_g are external sources and τ_1 is the GL relaxation time representing the dependence of elastic behavior on the temperature rate. The subscript "i" represents a spatial derivative, and a dot above a variable denotes a time derivative. Zhou *et al.* [28] considered $\epsilon = 1$, i.e., (1) is an LS theory. λ is the Lamé constant of the drained matrix, μ is its shear modulus, γ is a parameter representing the proportion of the matrix suction that contributes to the effective stress, which is supposed to be identical to the saturation S^l as an approximation [28], and α is the Biot effective-stress coefficient, which is given by

$$\alpha = 1 - K_b/K_s \tag{2}$$

with K_s the bulk modulus of the grains and $K_b = \lambda + 2\mu/3$, and $\beta_s = 3\ K_b\beta_T$ with β_T the thermal expansion coefficient. The other parameters in (1) are introduced in Appendix A.

The dynamical equations are

$$\begin{cases} \sigma_{xx,x} + \sigma_{xz,z} = \rho\dot{v}_x + \rho_l\dot{w}_x^{(l)} + \rho_g\dot{w}_x^{(g)} + f_x \\ \sigma_{xz,x} + \sigma_{zz,z} = \rho\dot{v}_z + \rho_l\dot{w}_z^{(l)} + \rho_g\dot{w}_z^{(g)} + f_z \\ -p_{l,x} = \rho_l\dot{v}_x + \dfrac{\rho_l}{\phi S^l}\dot{w}_x^{(l)} + \dfrac{\mu_l}{\kappa_r^l\kappa}w_x^{(l)} \\ -p_{l,z} = \rho_l\dot{v}_z + \dfrac{\rho_l}{\phi S^l}\dot{w}_z^{(l)} + \dfrac{\mu_l}{\kappa_r^l\kappa}w_z^{(l)} \\ -p_{g,x} = \rho_g\dot{v}_x + \dfrac{\rho_g}{\phi S^g}\dot{w}_x^{(g)} + \dfrac{\mu_g}{\kappa_r^g\kappa}w_x^{(g)} \\ -p_{g,z} = \rho_g\dot{v}_z + \dfrac{\rho_g}{\phi S^g}\dot{w}_z^{(g)} + \dfrac{\mu_g}{\kappa_r^g\kappa}w_z^{(g)} \end{cases} \tag{3}$$

where ϕ is the porosity, f_x and f_z are external forces, κ is the intrinsic permeability, ρ_l and ρ_g are the densities of liquid and gas, respectively, and

$$\rho = (1-\phi)\rho_s + \phi S^l\rho_l + \phi S^g\rho_g \tag{4}$$

is the composite density, with ρ_s the density of the grains. Parameters μ_l and μ_g and κ_r^l and κ_r^g are the dynamic viscosities and relative permeabilities of the liquid and gas, respectively, which are given in Appendix A.

Zhou *et al.* [28] derived a modified heat-conduction equation based on the dual-phase-lag model, which becomes the classic Fourier law when the phase-lag parameter related to the gradient of temperature becomes zero. In the present work, we consider the classic Fourier heat conduction equation for simplification

$$K\nabla^2 T = c(\dot{T} + \tau_q \ddot{T}) + \beta_s T_0(\epsilon_m + \epsilon\tau_q\dot{\epsilon}_m) - \beta_T T_0(\dot{p} + \epsilon\tau_q\ddot{p}) + q \tag{5}$$

where q is the heat source, K is the thermal conductivity, τ_q is the phase lag of the heat flux, c is the specific heat per unit volume in the absence of deformation

$$c = (1-\phi)\rho_s c_s + \phi S^l \rho_l c_l + \phi(1-S^l)\rho_g c_g \tag{6}$$

where c_i, $i = s, l, g$, is the specific heat capacity of phase i and ∇^2 is the Laplacian operator.

By using (1) and after a simplification, we obtain

$$\begin{aligned} K\nabla^2 T &= c(\dot{T} + \tau_q\ddot{T}) + d_1(\dot{T} + (1-\epsilon)\tau_1\ddot{T} + \epsilon\tau_q\ddot{T}) \\ &\quad + d_2(\epsilon_m + \epsilon\tau_q\dot{\epsilon}_m) + d_3(\epsilon_l + \epsilon\tau_q\dot{\epsilon}_l) \\ &\quad + d_4(\epsilon_g + \epsilon\tau_q\dot{\epsilon}_g) + q \end{aligned} \tag{7}$$

where

$$\begin{cases} d_1 = \beta_T T_0 \gamma a_{14} + \beta_T T_0(1-\gamma)a_{24} \\ d_2 = \beta_s T_0 + \beta_T T_0\gamma a_{11} + \beta_T T_0(1-\gamma)a_{21} \\ d_3 = \beta_T T_0\gamma a_{12} + \beta_T T_0(1-\gamma)a_{22} \\ d_4 = \beta_T T_0\gamma a_{13} + \beta_T T_0(1-\gamma)a_{23}. \end{cases} \tag{8}$$

Equations (1) and (7) are the generalization of the partially saturated porothermoelasticity theory proposed by Zhou *et al.* [28], including the GL and LS models. The first is obtained with $\epsilon = 0$, whereas the second with $\epsilon = 1$. Moreover, as stated by Ignaczak and Ostoja-Starzewski [31, p. 23], for the GL model, the relation $\tau_1 \geq \tau_q \geq 0$ holds.

III. Particle Velocity–Stress–Temperature Formulation and Algorithm

In order to facilitate the simulation of wavefields, we recast (3) as follows:

$$\begin{cases} \dot{v}_x = \beta_{11}(\sigma_{xx,x} + \sigma_{xz,z} - f_x) - \beta_{12}(p_{l,x} + b_l w_x^{(l)}) \\ \quad -\beta_{13}(p_{g,x} + b_g w_x^{(g)}) = \mathrm{II}_x \\ \dot{v}_z = \beta_{11}(\sigma_{xz,x} + \sigma_{zz,z} - f_z) - \beta_{12}(p_{l,z} + b_l w_z^{(l)}) \\ \quad -\beta_{13}(p_{g,z} + b_g w_z^{(g)}) = \mathrm{II}_z \\ \dot{w}_x^{(l)} = \beta_{21}(\sigma_{xx,x} + \sigma_{xz,z} - f_x) - \beta_{22}(p_{l,x} + b_l w_x^{(l)}) \\ \quad -\beta_{23}(p_{g,x} + b_g w_x^{(g)}) = \Omega_x \\ \dot{w}_z^{(l)} = \beta_{21}(\sigma_{xz,x} + \sigma_{zz,z} - f_z) - \beta_{22}(p_{l,z} + b_l w_z^{(l)}) \\ \quad -\beta_{23}(p_{g,z} + b_g w_z^{(g)}) = \Omega_z \\ \dot{w}_x^{(g)} = \beta_{31}(\sigma_{xx,x} + \sigma_{xz,z} - f_x) - \beta_{32}(p_{l,x} + b_l w_x^{(l)}) \\ \quad -\beta_{33}(p_{g,x} + b_g w_x^{(g)}) = \Gamma_x \\ w_z^{(g)} = \beta_{31}(\sigma_{xz,x} + \sigma_{zz,z} - f_z) - \beta_{32}(p_{l,z} + b_l w_z^{(l)}) \\ \quad -\beta_{33}(p_{g,z} + b_g w_z^{(g)}) = \Gamma_z \end{cases} \tag{9}$$

where $b_l = \mu_l/(\kappa_r^l \kappa)$, $b_g = \mu_g/(\kappa_r^g \kappa)$

$$\begin{bmatrix} \beta_{11} & \beta_{12} & \beta_{13} \\ \beta_{21} & \beta_{22} & \beta_{23} \\ \beta_{31} & \beta_{32} & \beta_{33} \end{bmatrix} = \frac{1}{N}\begin{bmatrix} -1 & \phi S^l & \phi S^g \\ \phi S^l & P & -\phi^2 S^g S^l \\ \phi S^g & -\phi^2 S^g S^l & Q \end{bmatrix} \tag{10}$$

where $N = \phi\rho_g S^g - \rho + \phi\rho_l S^l$, $P = -\phi S^l(\rho - \phi\rho_g S^g)/\rho_l$, $Q = -\phi S^g(\rho - \phi\rho_l S^l)/\rho_g$.

Defining

$$\dot{T} = \psi \tag{11}$$

(7) becomes

$$\begin{aligned} \dot{\psi} &= \frac{1}{L}[K\nabla^2 T - d_2[\epsilon_m + \epsilon\tau_q(\mathrm{II}_{x,x} + \mathrm{II}_{z,z})] \\ &\quad - d_3[\epsilon_l + \epsilon\tau_q(\Omega_{x,x} + \Omega_{z,z})] - d_4[\epsilon_g + \epsilon\tau_q(\Gamma_{x,x} + \Gamma_{z,z})]] \\ &\quad - \frac{c + d_1}{L}\psi - \frac{q}{L} \end{aligned} \tag{12}$$

where $L = c\tau_q + d_1(1-\epsilon)\tau_1 + \epsilon\tau_q d_1$.

Equations (9), (11), and (12) together with (1) constitute the velocity–stress–temperature formulation, which is the basis of wavefield simulation. A corresponding plane-wave analysis to obtain the phase velocities and attenuation factors is given in Appendix B.

A. Numerical Algorithm

The 2-D equations can be written in matrix form as

$$\dot{\mathbf{v}} + \mathbf{s} = \mathbf{M}\cdot\mathbf{v} \tag{13}$$

where

$$\mathbf{v} = [v_x, v_z, w_x^{(l)}, w_z^{(l)}, w_x^{(g)}, w_z^{(g)}, \sigma_{xx}, \sigma_{zz}, \sigma_{xz}, p_l, p_g, T, \psi]^{\mathrm{T}} \tag{14}$$

is the unknown array vector

$$\mathbf{s} = [-\beta_{11}f_x, -\beta_{11}f_z, -\beta_{21}f_x, -\beta_{21}f_z, -\beta_{31}f_x, -\beta_{31}f_z \\ f_{xx}, f_{zz}, f_{xz}, -f_l, -f_g, 0, -q/L]^{\mathrm{T}} \tag{15}$$

is the source vector and $\mathbf{M}$ is the propagation matrix. Following [26], the solution to (13), subject to the initial condition $\mathbf{v}(0) = \mathbf{v}_0$, is:

$$\mathbf{v}(t) = \exp(t\mathbf{M})\mathbf{v}_0 + \int_0^t \exp(\tau\mathbf{M})\mathbf{s}(t-\tau)d\tau \tag{16}$$

where $\exp(t\mathbf{M})$ is the evolution operator.

The eigenvalues of $\mathbf{M}$ may have negative real parts and differ greatly in magnitude, due to the presence of the viscosity term and relaxation time in the heat equation [26], indicating that the problem is stiff. The presence of positive real eigenvalues creates instabilities in explicit time-integration methods. Carcione *et al.* [26] solved the thermoporoelasticity equations by using a splitting or partition method, where both the stiffness and instability problems are solved by calculating the unstable part of the equations analytically. The equations are solved by a direct-grid algorithm, based on the Fourier pseudospectral method for computing the spatial derivatives and the Runge–Kutta time-integration technique. Alternatively, they also proposed a Crank–Nicolson time-stepping scheme. In Appendix C, we derive this scheme adapted to the partially saturated thermoporoelasticity theory. The spatial derivatives are calculated with the optimized FD method [29]. The perfectly matched layer (PML) technique is used to prevent boundary reflections when the wavefront exceeds the size of the model.

TABLE I
MEDIUM PROPERTIES

Parameters	K_s (GPa)	λ (GPa)	ρ_s (kg/m^3)	S^l	S^l_{sat}	μ (GPa)	c_s (kg/(m s^2 °K))	β_{wp} (Pa^{-1})	β_ψ (°K^{-1})
Values	35	4	2650	0.6	1.0	1.5	100	4.58 ×10^{-10}	2.09×10^{-3}
Parameters	κ (darcy)	χ (Pa^{-1})	ρ_l (kg/m^3)	ϕ	p^*_g (kPa)	S^l_{res}	c_l (kg/(m s^2 °K))	β_{sT} (°K^{-1})	
Values	1	0.0001	1000	0.4	101.3	0.05	418	7.8 ×10^{-6}	
Parameters	m	d	ρ_g (kg/m^3)	T_b (°K)	T_0 (°K)	β_T (°K^{-1})	c_g (kg/(m s^2 °K))	β_{wT} (°K^{-1})	
Values	0.5	2	1.3	300.2	300	1×10^{-4}	190	2.1 ×10^{-4}	
Case 1	τ_q (ns)	τ_1 (ns)	K (m kg/(s^3 °K))	*Case 2*	τ_q (s)	τ_1 (s)	K (m kg/(s^3 °K))		
	0.08	0.16	12		0.008	0.016	12 ×10^8		

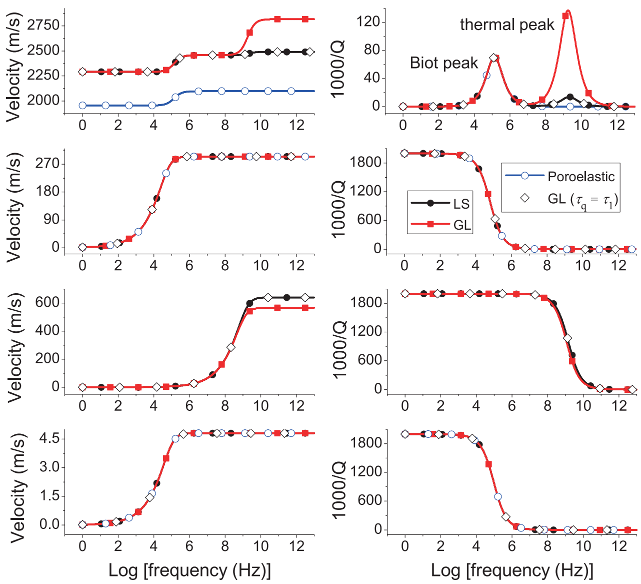

Fig. 1. Phase velocity (Left) and dissipation factor (Right) of the four compressional modes (P1, P2, T, and P3, respectively, from up to down) as a function of frequency. The black and red lines correspond to the LS and GL models, whereas the diamonds indicate the result of GL when $\tau_1 = \tau_q$. The blue line is the result of the classic poroelasticity theory. The medium properties are given in Table I (Case 1).

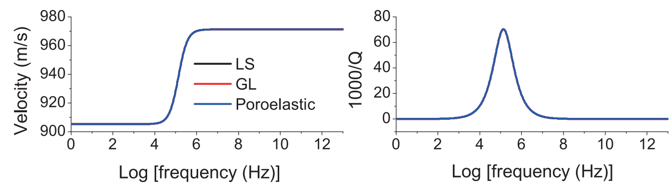

Fig. 2. Phase velocity (Left) and dissipation factor (Right) of the shear wave. The three curves, representing the results of the partially saturated LS, GL, and poroelasticity theories, overlap. The medium properties are given in Table I (Case 1).

IV. EXAMPLES

We consider the medium properties given in Table I, where we use smaller heat capacities c_i than [28] to highlight the thermal wave and choose two different cases regarding the thermoelasticity properties. The parameters of Case 1 correspond to a typical rock, whereas those of Case 2 may refer to a hypothetical synthetic material. The main objective is to show the behavior for different values of the thermal conductivity to better illustrate the physics.

A. Case 1

Figs. 1 and 2 show the phase velocities and dissipation factors of the five wave modes as a function of frequency. The fast P1 wave has two relaxation peaks, at 100 kHz and 1 GHz, induced by the Biot mechanism and the thermal effect, respectively. The former results in a strong velocity dispersion of the P2 and P3 waves around 100 kHz, whereas the latter is related to dispersion of the thermal wave at high frequencies. When $\tau_1 > \tau_q$ (the red line), the GL model predicts a higher P1-wave thermal attenuation than the LS one and, consequently, more velocity dispersion, which implies a higher velocity at high frequencies. The opposite behavior for the T wave occurs at these frequencies. Both models give higher P1-wave velocities than the classic poroelasticity theory. If $\tau_1 = \tau_q$, the two models coincide, in agreement with the classical thermoelastic model [30]. The slow waves have a similar characteristic as the T wave, with diffusive and wavelike behaviors at low and high frequencies, respectively, and they are hardly affected by the thermal effect. As shown in Appendix B, the shear wave is not thermally affected, and hence, its propagation remains the same as that of the classical poroelasticity theory.

The wavefield simulation based on the Crank–Nicolson algorithm given in Appendix C is then carried out. We consider a model with a 600 × 600 mesh. The source is located at the center of the model and has the time history

$$h(t) = \cos[2\pi(t - t_0) f_0]\exp[-2(t - t_0)^2 f_0^2] \qquad (17)$$

where f_0 is the central frequency and $t_0 = 3/(2 f_0)$ is a time delay to make the signal causal.

Fig. 3 shows the simulated snapshots at 0.65 ns for $f_0 =$ 10 GHz, where we consider a grid spacing $dx = dz =$ 0.005 μm and a time step $dt = 0.5 \times 10^{-3}$ ns. In agreement with the plane-wave analysis, the P1, P2, and T waves are wavelike and can be recognized. The GL model predicts a higher P1-wave velocity and stronger attenuation, yielding a more attenuated P1-wave wavefront. The P2 wave has a lower propagation velocity than the T wave, and it does not evidently depend on the type of model (LS or GL) and can be more clearly observed in the $w_z^{(l)}$ and $w_z^{(g)}$ snapshots. The T wave of the LS model has a higher velocity than that of the GL model and can be significantly observed in the

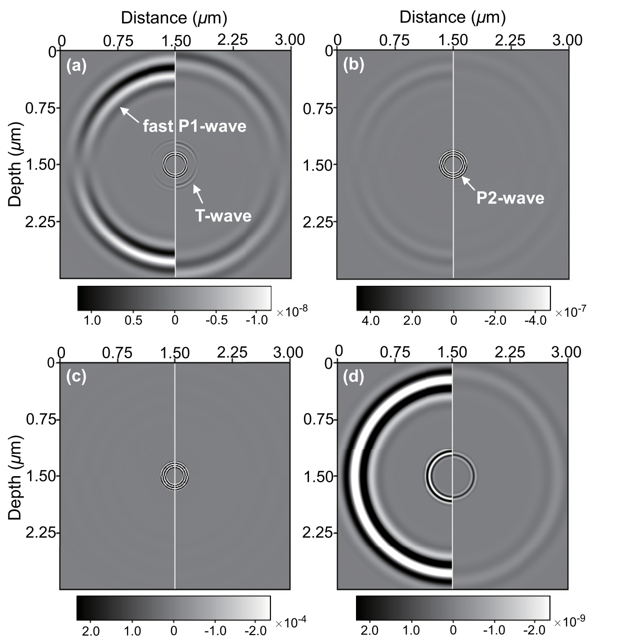

Fig. 3. Snapshots of (a) v_z, (b) $w_z^{(l)}$, (c) $w_z^{(g)}$, and (d) T at 0.65 ns. The sources are dilatational (f_{xx}, f_{zz}, f_l, and f_g) with a central frequency of 10 GHz, and the properties are those of Case 1. In each panel, the left and right parts show the results of the LS and GL models, respectively.

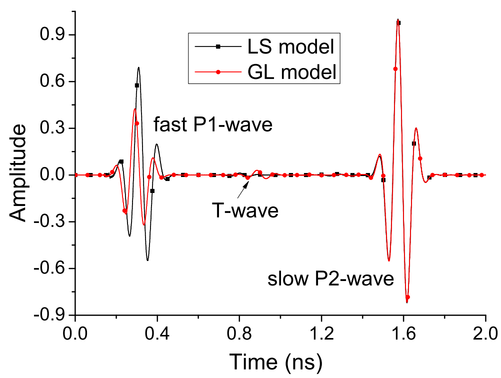

Fig. 4. Waveform of v_z at (1.2, 1.2) μm corresponding to Fig. 3. The black and red lines represent the results of the LS and GL models, respectively. Fields are normalized.

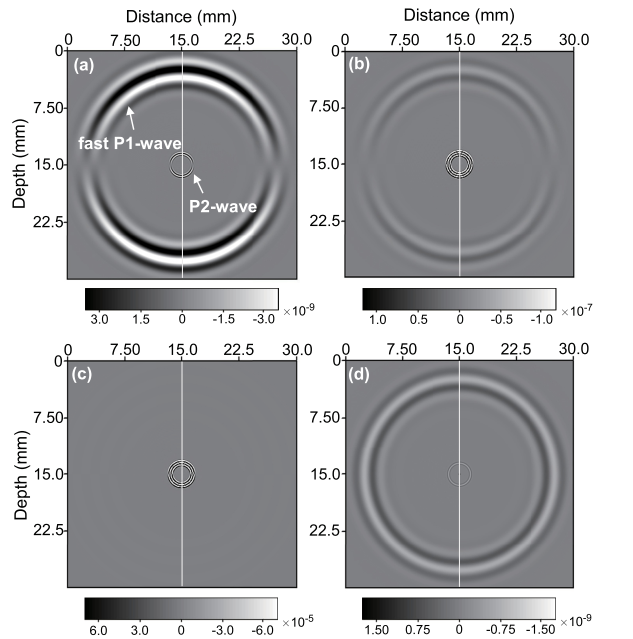

Fig. 5. Snapshots of (a) v_z, (b) $w_z^{(l)}$, (c) $w_z^{(g)}$, and (d) T at 6.5 μs. The sources are dilatational with a central frequency of 1 MHz, and the properties are those of Case 1. In each panel, the left and right parts show the results of the LS and GL models, respectively.

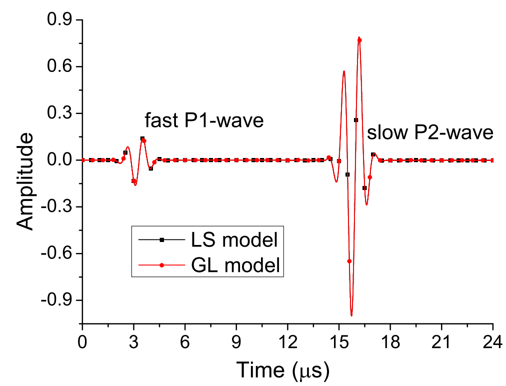

Fig. 6. Waveform of $w_z^{(l)}$ at (12, 12) mm corresponding to Fig. 5. The black and red lines overlap, representing the results of the LS and GL models, respectively.

T-component snapshot. The P3 wave does not propagate due to the very low velocity.

The corresponding v_z-component waveform at (1.2, 1.2) μm is shown in Fig. 4. The P2-wave waveform remains unchanged for both the LS and GL models, with the latter predicting a faster propagation but stronger loss of the P1 wave. The reverse trend occurs for the T wave. These results are in agreement with the plane-wave analysis as expected. Fig. 5 similarly shows the results for $f_0 = 1$ MHz, where we consider a grid spacing $dx = dz = 0.05$ mm and a time step $dt = 5$ ns. Only the P1 and P2 waves are wavelike and their behaviors are the same for both models, as shown in Fig. 1. The T wave does not propagate and can be seen in the T snapshot at the source location. The $w_z^{(l)}$ waveforms at (12, 12) mm shown in Fig. 6 further validate these conclusions. If $f_0 = 100$ Hz, only the fast P1 wave propagates (see Fig. 1), which is not affected by the thermal effect. This can be confirmed by the v_z-component snapshot in Fig. 7, where we use a grid spacing $dx = dz = 0.5$ m and a time step $dt = 0.05$ ms.

B. Case 2

The corresponding velocity and dissipation factor for this case are shown in Figs. 8 and 9. A comparison with Figs. 1 and 2 indicates that using a higher K (or relaxation time), the thermal peak moves to low frequencies. The main velocity dispersion occurs at the frequency range [1, 100] Hz, which corresponds to the exploration-geophysics band. A similar phenomenon in fully saturated porothermoelastic media was studied in [26]. The Biot peak remains unchanged, causing velocity dispersion of both the P1 and P2 waves

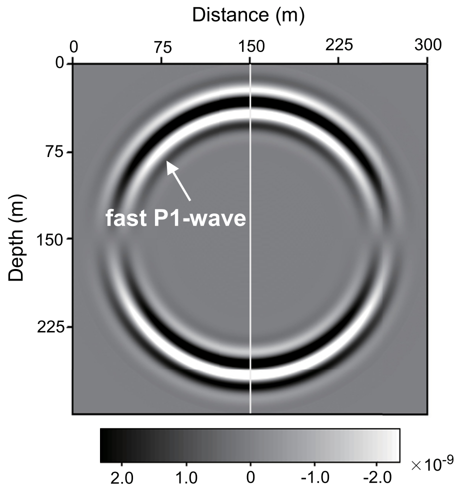

Fig. 7. Snapshots of v_z at 0.065 s. The sources are dilatational with a central frequency of 100 Hz and the properties are those of Case 1. (Left and Right) Results of the LS and GL models, respectively.

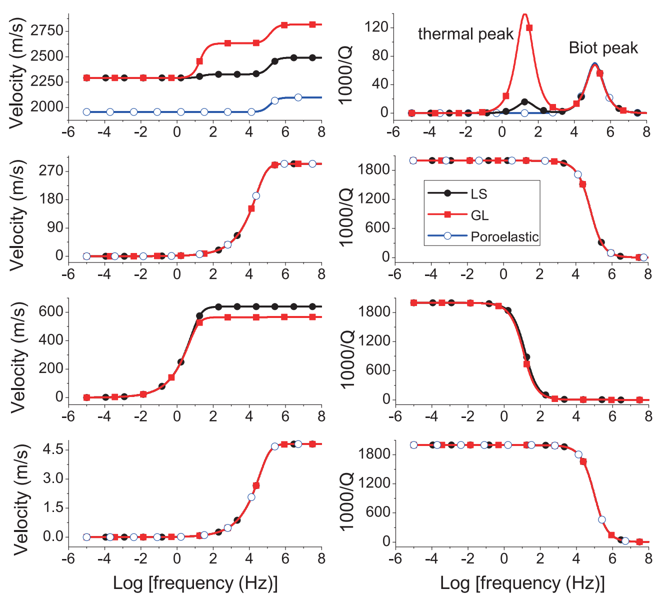

Fig. 8. Phase velocity (Left) and dissipation factor (Right) of the compressional modes (P1, P2, T, and P3 waves, respectively, from up to down) as a function of frequency. The black and red lines correspond to the LS and GL models, whereas the blue line is the result of partially saturated poroelasticity theory. The medium properties are given in Table I (Case 2).

around 100 kHz. The LS model gives a lower P1-wave velocity but a higher T-wave velocity for frequencies beyond 10 Hz, similar to those of Case 1 at high frequencies. The two models exhibit higher P1-wave velocities than the poroelasticity theory for all frequencies, as in Case 1. The behaviors of the P2 and P3 waves are not evidently affected by the thermal effects. The shear wave is not affected by the thermal effects, and hence, its propagation, for both LS and GL models, is the same as that of the classical poroelasticity theory.

Next, wavefield simulations are performed. The results at 100 Hz are shown in Fig. 10, where we only observe the P1 and T waves, in agreement with the plane-wave analysis.

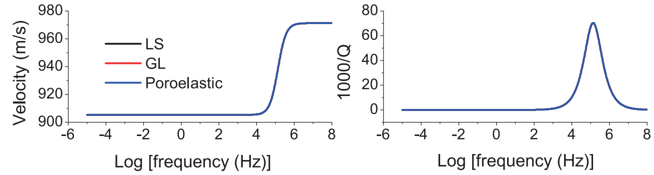

Fig. 9. Phase velocity (Left) and dissipation factor (Right) of the shear wave. The three curves with different colors representing the results of partially saturated LS, GL, and poroelastic models overlap. The medium properties are given in Table I (Case 2).

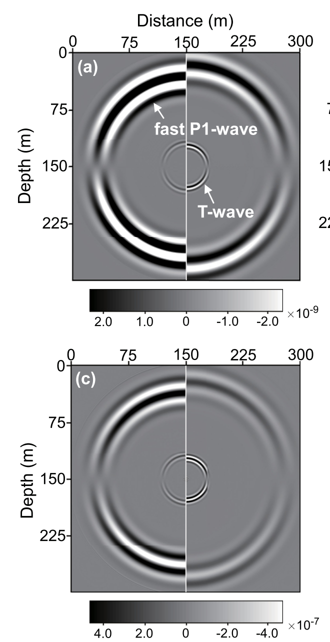

Fig. 10. Snapshots of (a) v_z, (b) $w_z^{(l)}$, and (c) $w_z^{(g)}$ at 0.065 s. The sources are dilatational with a central frequency of 100 Hz and the properties are those of Case 2. In each panel, the left and right parts show the results of the LS and GL models, respectively.

The modeling parameters are the same as those used in Fig. 7. The P1-wave wavefront of the GL model propagates faster but exhibits more attenuation than that of the LS model. The opposite trend is noted for the T wave. The v_z waveform at (120, 120) m shown in Fig. 11 further validates this analysis.

The results with 1 MHz are given in Fig. 12, where we observe all the P1, P2, and T waves. The P2 wave is the slowest and can be identified as the inner wavefront, particularly in the $w_z^{(l)}$ and $w_z^{(g)}$ snapshots. It remains the same for the two models, in agreement with the plane-wave analysis. The characteristics of P1 and T waves are similar to those shown in Fig. 10. The $w_z^{(l)}$ waveform at (12, 12) mm shown in Fig. 13 confirms these results.

To complete the analysis for wave propagation in homogeneous media, Fig. 14 shows the snapshot of $\omega_z^{(g)}$ at a propagation time of 6.5 μs, where the P1, P2, T, and S waves are present. The field is obtained by using a shear source (f_{xz}) with 1-MHz dominant frequency and the properties are the same as those in Fig. 12. The S wave is not coupled to the heat equation, but because the shear source generates P-wave energy, the two wave modes appear simultaneously.

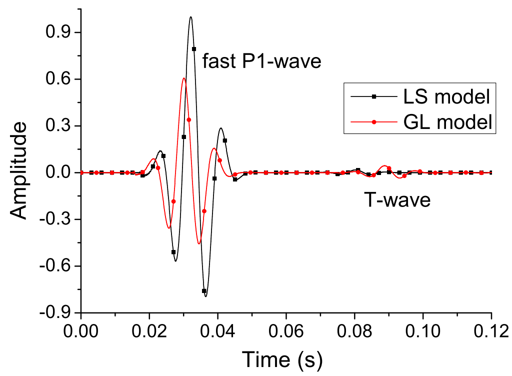

Fig. 11. Waveform of v_z at (120, 120) m corresponding to Fig. 10. The black and red lines represent the results of the LS and GL models, respectively.

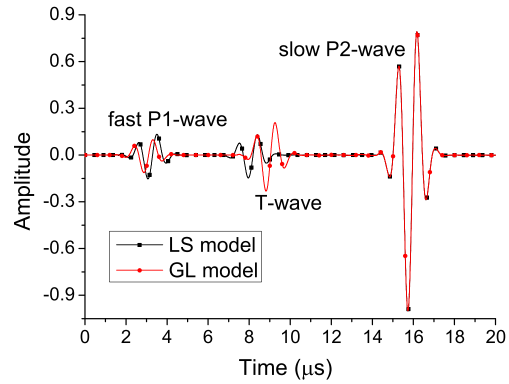

Fig. 13. Waveform of $w_z^{(l)}$ at (12, 12) mm corresponding to Fig. 12. The black and red lines represent the results of the LS and GL models, respectively.

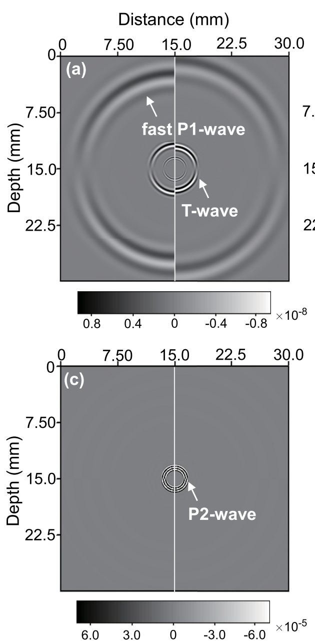

Fig. 12. Snapshots of (a) v_z, (b) $w_z^{(l)}$, and (c) $w_z^{(g)}$, at 6.5 μs. The sources are dilatational with a central frequency of 1 MHz and the properties are those of Case 2. In each panel, the left and right parts show the results of the LS and GL models, respectively.

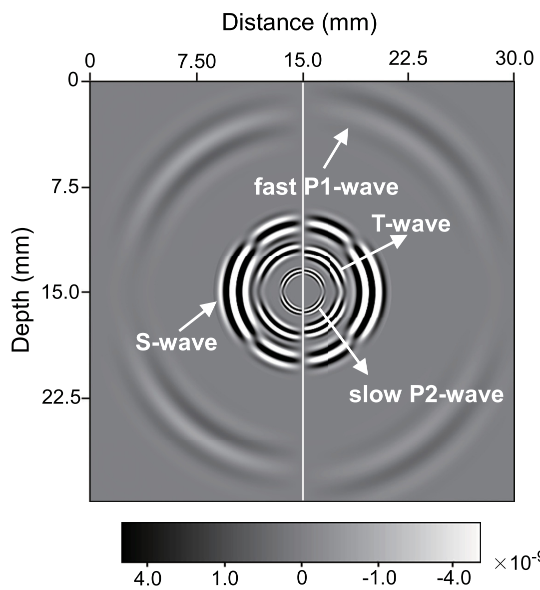

Fig. 14. Snapshot of $w_z^{(g)}$ at 6.5 μs, where a shear source with a central frequency of 1 MHz is used. The properties are those of Case 2. The left and right parts show the results of the LS and GL models, respectively.

Indeed, energy conversion between the shear and P-wave modes occurs in the case of heterogeneity, due to the reflection and transmission phenomenon.

C. Effect of Fluid Saturation

Saturation plays an essential role in wave propagation in rocks. Fig. 15 shows the velocities and dissipation factors as a function of frequency for three saturations. The results are obtained by using the GL model with the parameters of Case 2. We observe that, for the given frequency, the P1-wave velocity increases with decreasing saturation. The Biot relaxation peak moves to high frequencies, the corresponding maximum attenuation decreases for decreasing saturation, the maximum thermal attenuation decreases as saturation increases, the T-wave velocity at high frequencies increases as the saturation decreases, and P3-wave dispersion moves to the high frequencies when saturation decreases.

Next, wavefields are computed. Fig. 16 shows the snapshots at 6.5 μs for 1 MHz, where we can observe the P1, P2, and T waves. With $S^l = 0.4$, the P1 wave propagates faster compared to $S^l = 0.6$, whereas it propagates slowest when $S^l = 0.8$. The propagation of the T wave varies with saturation in a similar manner as that of the P1 wave. The slow P2 wave can be recognized as the innermost wavefront and it is hardly affected by the saturation. Fig. 17, showing the $w_z^{(l)}$ waveform at (12, 12) mm, confirms the above conclusions. The P1 wave is mostly attenuated and propagates with the highest velocity when $S^l = 0.4$. All these results are in agreement with the dispersion analysis in Fig. 15.

Fig. 18 shows the results for $f_0 = 100$ Hz. In this case, both the P2 and P3 waves are dissipative. The P1 and T waves propagate with the highest velocities when $S^l = 0.4$ and those with $S^l = 0.8$ exhibit the smallest. The corresponding

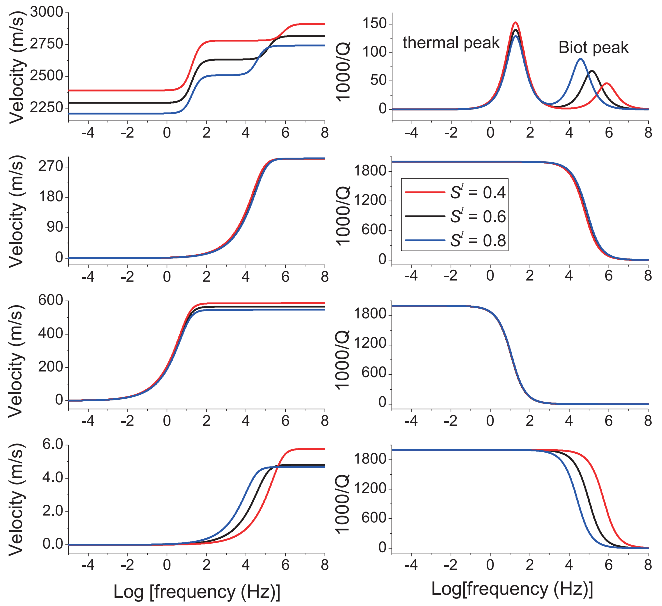

Fig. 15. Phase velocity (Left) and dissipation factor (Right) as a function of frequency, calculated with the GL model and three saturations. (From Top to Bottom) Results of P1, P2, T, and P3 waves, respectively. The medium properties are given in Table I (Case 2).

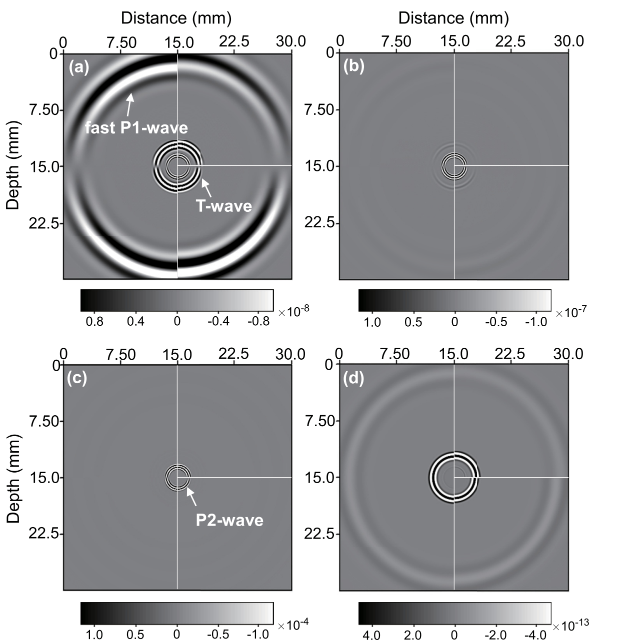

Fig. 16. Snapshots of (a) v_z, (b) $w_z^{(l)}$, (c) $w_z^{(g)}$, and (d) T at 6.5 μs. The sources are dilatational with a central frequency of 1 MHz and the properties are those of Case 2. (Left, Top Right, and Bottom Right) Results of the GL model with $S^l = 0.6$, 0.4 and 0.8, respectively.

v_z waveform at (120, 120) m shown in Fig. 19 confirms this behavior.

D. Heterogeneous Media

Finally, we present an example of a heterogeneous two-layer model. The upper medium has $\lambda = 2.5$ GPa and $\mu = 1.2$ GPa,

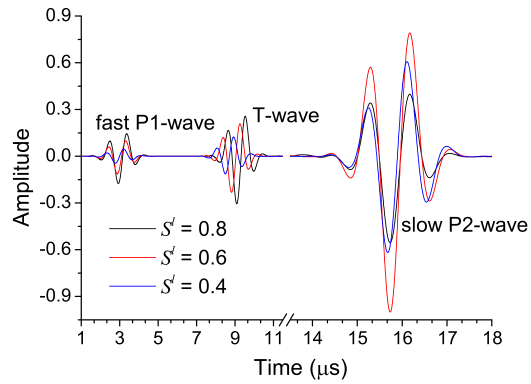

Fig. 17. Waveform of $w_z^{(l)}$ at (12, 12) mm corresponding to Fig. 16.

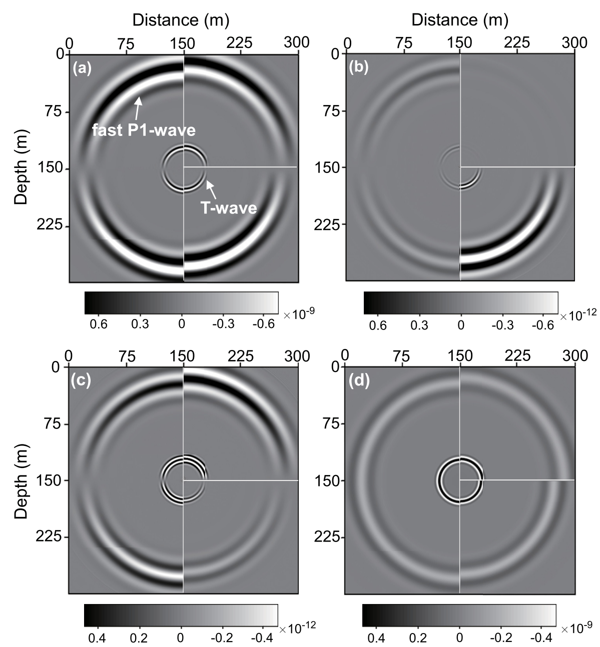

Fig. 18. Snapshots of (a) v_z, (b) $w_z^{(l)}$, (c) $w_z^{(g)}$, and (d) T at 0.065 s. The sources are dilatational with a central frequency of 100 Hz and the properties are those of Case 2. (Left, Top Right, and Bottom Right) Results of the GL model with $S^l = 0.6$, 0.4, and 0.8, respectively.

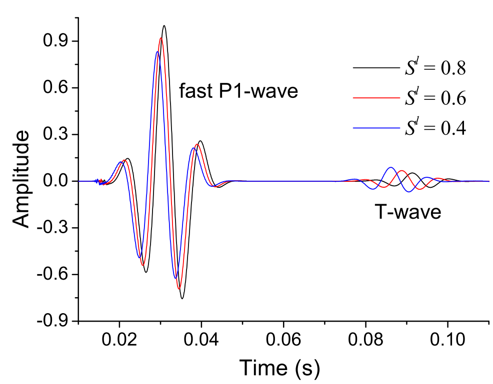

Fig. 19. Waveform of v_z at (120, 120) m corresponding to Fig. 18.

whereas the lower has $\lambda = 4.0$ GPa and $\mu = 1.5$ GPa. The other properties are the same as those in Table I (Case 2). We consider a model with 800 $\times$ 800 grid points and assume

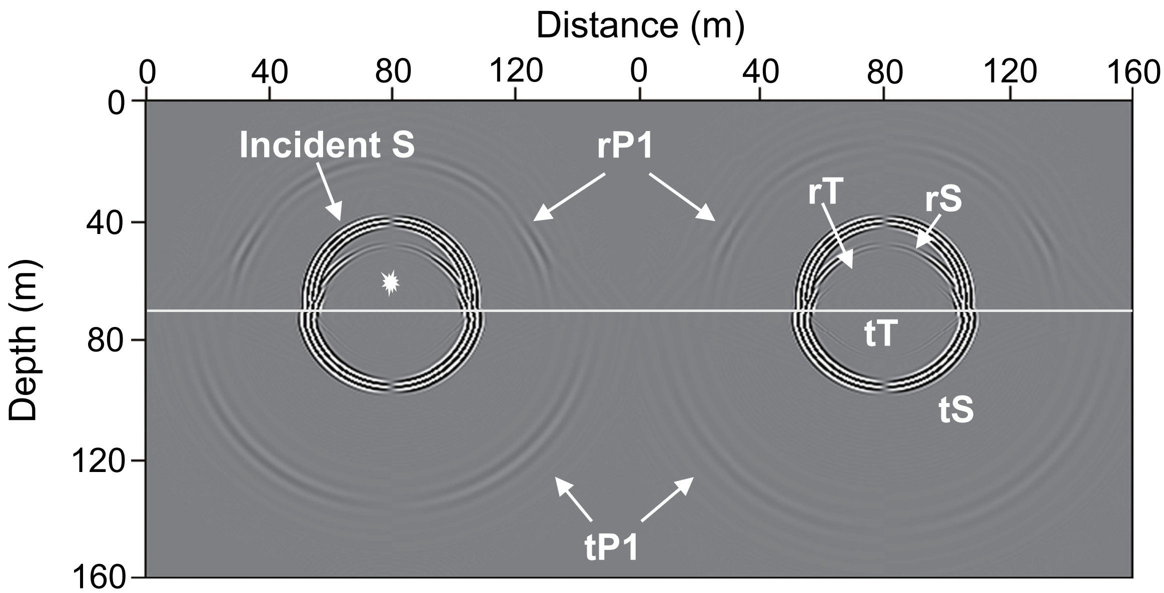

Fig. 20. Snapshots of v_z, at 0.036 s for the two-layer model. (Left and Right) Results of the LS and GL models, respectively. The incident, reflected (r), and transmitted (t) P1, S, and T waves can be observed.

that the interface is vertically located at the 355th grid. The source is pure shear with $f_0 = 400$ Hz, which can be easily implemented by replacing f_x and f_z in (9) with $\partial_z f(x,z,t)$ and $-\partial_x f(x,z,t)$, respectively, where

$$f(x,z,t) = \exp\left[-\sqrt{\eta^2\left((x-x_0)^2+(z-z_0)^2\right)}\right]h(t) \quad (18)$$

where $\eta = 10$ is the attenuation coefficient and (x_0, z_0) is the source location. Basically, the aim is to study the T wave converted from the incident S wave at the interface and discuss the coupling of the shear wave in heterogeneous media.

Fig. 20 shows the v_z-component snapshot at 0.036 s, where we consider $dx = dz = 0.2$ m and $dt = 0.03$ ms. Apart from the reflected and transmitted P1 and S waves, the incident S wave also generates converted T waves in both layers, which can be recognized as the innermost wavefront that has a relatively weak energy and small propagation velocity. The fast P1 wave in the case of the GL model propagates faster but is more attenuated, whereas the propagation of the T wave is opposite, in agreement with the analyses in the homogeneous case. In particular, the reflected T wave of the LS model has a very weak energy and can hardly be seen. Even though the S wave is not coupled with the heat equation, its propagation in heterogeneous media causes energy conversion to the T wave and can induce new energy loss.

V. Discussion

When seismic waves propagate through heterogeneous rocks, pressure gradients between regions of dissimilar properties occur [18]. This induces an internal equilibration with fluid flowing from the more compliant high-pressure regions to the low-pressure regions, which generates mode conversion from the fast P wave to Biot slow waves, accompanied by wave-induced fluid-flow attenuation [17]. Based on the scales of the heterogeneities, the flow is squirt flow or mesoscopic flow [31]. The squirt flow occurs at the microscopic scale and describes attenuation mainly at ultrasonic frequencies, whereas the mesoscopic flow is dominant at the mesoscopic scale, i.e., a scale larger than the pore size but smaller than the wavelength, which is considered as the main cause of high attenuation of low-frequency elastic waves. Further studies involve incorporating these two attenuation mechanisms.

The process of thermal attenuation is similar to that of wave-induced fluid flow [21]. When the porous rocks are thermally insulated, the passage of a P wave induces temperature variations (gradient), and conversion to thermal wave, which introduces a new loss mechanism that can be termed wave-induced thermo-poroelastic attenuation, in analogy with wave-induced fluid-flow attenuation. The main difference is that the thermal propagation is governed by the Fourier heat equation, and hence, its relaxation frequency is dependent on the thermal properties. Following [25], the thermal relaxation frequency is inversely proportional to the conductivity and moves to the low frequency when K increases. For typical materials, K ranges from 24000 m kg/(s^3 °K) for CRC aluminum to 0.023 m kg/(s^3 °K) for air, whereas rocks filled with fluids have a range between 1 and 12 m kg/(s^3 °K). Therefore, in typical rocks, the thermal wave is dissipative and does not propagate at low frequencies, such as the exploration-geophysics band (see Case 1), similar to the Biot slow wave. However, the fact that these waves are diffusive is the cause of attenuation of the fast P wave. The temperature-related wave can be observed in either material with high-thermal conductivity or over high-frequency bands. For example, McNelly *et al.* [32] verified the existence of the T wave in NaF crystals experimentally, whereas Huberman *et al.* [33] observed the temperature-related wave in graphite above 100 °K.

The present model predicts a single shear wave and its loss is not affected by the thermal variation. The basic reason is that the model assumes no couplings between the shear stress and the temperature rate since the Fourier heat conduction equation does not involve shear strain. The shear wave has a different polarization than the compressional wave, and hence, the corresponding governing equations must be different, an analysis to be performed in future work.

VI. Conclusion

We have proposed a theory and numerical simulation for wave propagation in partially saturated porothermoelastic media, including the LS and GL models. The theory predicts five wave modes, namely, the fast P wave, the S wave, two slow P waves (P2 and P3), and a thermal wave. This mode is coupled with the P waves, inducing additional energy dissipation. The slow P2 and thermal waves are diffusive at low frequencies and wavelike at high frequencies, whereas the slow P3 wave propagates with a very small velocity at all frequencies. The GL model can predict more attenuation and consequently larger dispersion of the fast P wave for a combination of relaxation times $\tau_1 > \tau_q$. The thermal relaxation peak moves to low frequencies when the conductivity increases, but the slow P waves are hardly affected. Decreasing saturation induces increased P-wave velocity and moves the Biot relaxation peak to high frequencies.

The numerical algorithm is based on an optimized staggered-grid FD method to compute the spatial derivatives and a Crank–Nicolson time-stepping scheme, which allows us to handle spatially inhomogeneous media and overcome stiff/instability problems. The simulated snapshots and waveforms corresponding to two different sets of thermoelastic properties illustrate the physics of wave propagation at different frequencies, which are in agreement with the plane-wave analysis. The methods will be extended to the case of two liquids and anisotropic and 3-D media in a future study and compared with other similar theories based on interfacial tension between the fluids, involving the concept of capillary pressure explicitly.

Appendix A
Parameters Involved

Following Zhou *et al.* [28], we have:

$$\begin{cases} A_{11} = \phi S^l \beta_{wp}, \quad A_{12} = \phi(1-S^l)\dfrac{M_a}{\rho_g R T_b} \\ A_{13} = 1-\phi, \quad A_{14} = \phi S^l, \quad A_{15} = \phi(1-S^l) \\ A_{16} = -(1-\phi)\beta_{sT} - \phi S^l \beta_{wT} - \phi(1-S^l)\dfrac{M_a p_g^*}{\rho_g R {T_b}^2} \end{cases} \tag{A.1}$$

$$\begin{cases} A_{21} = \phi S^l(1-S^l)\beta_{wp} - \phi A_s \\ A_{22} = \phi A_s - \phi S^l(1-S^l)\dfrac{M_a}{\rho_g R T_b}, \quad A_{23} = 0 \\ A_{24} = -A_{25} = \phi S^l(1-S^l) \\ A_{26} = -\phi \beta_\psi A_s \chi^{-1}\left(S_e^{-\frac{1}{m}} - 1\right)^{\frac{1}{d}} \\ \quad + \phi S^l S^g\left(\dfrac{M_a p_g^*}{\rho_g R T_b^2} - \beta_{wT}\right) \end{cases} \tag{A.2}$$

where ϕ is the porosity, β_{wp} and β_{wT} are the compressibility and thermal-expansion coefficients of the fluid, respectively, β_{sT} denotes the thermal-expansion coefficient of the solid, and $M_a = 0.0288$ kg/mol is the molar mass of dry air. $R = 8.3144$ J/mol/°K is the universal gas constant, ρ_g is the density of the gas, and β_ψ is a surface tension-temperature-dependent coefficient. p_g^* is the gas pressure, whereas T_b is the internal temperature related to the gas described by the ideal gas law [34], which mainly affects the Biot attenuation induced by the saturated fluids. Here, the two properties are set as 300.2 °K and 101.3 kPa, respectively. The three independent parameters χ, m, and d correspond to the V-G (Van Genuchten) model, which can be determined by fitting the soil–water retention model to the experimental data. Following [35], $m = 1 - 1/d$ is used. S_e is the effective water saturation given by [35]:

$$S_e = \left(S^l - S^l_{res}\right)/\left(S^l_{sat} - S^l_{res}\right). \tag{A.3}$$

With the above definitions, A_s is obtained as

$$A_s = -\chi m d\left(S^l_{sat} - S^l_{res}\right) S_e^{(m+1)/m}\left(S_e^{-1/m} - 1\right)^{1-1/d}. \tag{A.4}$$

With (A.1) and (A.2), we have [28]

$$\begin{cases} a_{11} = \dfrac{A_{22}}{G}, \quad a_{12} = \dfrac{A_{22}A_{14} - A_{12}A_{24}}{G\phi S^l} \\ a_{13} = \dfrac{A_{22}A_{15} - A_{12}A_{25}}{G\phi S^g}, \quad a_{14} = \dfrac{A_{22}A_{16} - A_{12}A_{26}}{G} \\ a_{21} = \dfrac{-A_{21}}{G}, \quad a_{22} = \dfrac{A_{11}A_{24} - A_{21}A_{14}}{G\phi S^l} \\ a_{23} = \dfrac{A_{11}A_{25} - A_{21}A_{15}}{G\phi S^g}, \quad a_{24} = \dfrac{A_{11}A_{26} - A_{21}A_{16}}{G} \end{cases} \tag{A.5}$$

where $G = A_{22}A_{11} - A_{12}A_{21}$.

The dynamic viscosities and relative permeabilities of the liquid and gas in (3) are [28]

$$\mu_l = (243.18 \times 10^{-7})10^{\frac{247.8}{T_b - 140}}, \quad \mu_g = 1.48 \times 10^{-6}\frac{\sqrt{T_b}}{1 + 119/T_b}$$
$$\kappa_r^l = \sqrt{S_e}\left[1 - (1 - S_e^{1/m})^m\right]^2, \quad \kappa_r^g = \sqrt{1 - S_e}(1 - S_e^{1/m})^{2m} \tag{A.6}$$

respectively.

Appendix B
Plane-Wave Analysis

Because the medium is isotropic, it is enough to consider a 1-D medium when performing the plane-wave analysis. In the 1-D case, the field vector becomes $\mathbf{v} = [v, w^{(l)}, w^{(g)}, \sigma, p_l, p_g, T]^{\mathrm{T}}$. In the following, we consider a plane-wave kernel $\exp[i(\omega t - kx)]$, where ω is the angular frequency and k is the complex wavenumber. The S wave is not thermally affected and its complex velocity is [28]

$$v_s = \sqrt{\frac{\mu}{\rho - \rho_g^2\left[\dfrac{\rho_g}{\phi S^g} + \dfrac{i\mu_g}{\omega\kappa_r^g\kappa}\right]^{-1} - \rho_l^2\left[\dfrac{\rho_l}{\phi S^l} + \dfrac{i\mu_l}{\omega\kappa_r^l\kappa}\right]^{-1}}}. \tag{B.1}$$

In the 1-D space, (1), (3), and (7) reduce to

$$\begin{cases} -k\sigma = \rho\omega v + \rho_l\omega w^{(l)} + \rho_g\omega w^{(g)} \\ kp_l = \rho_l\omega v + \dfrac{\rho_l}{\phi S^l}\omega w^{(l)} - \dfrac{i\mu_l}{\kappa_r^l\kappa}w^{(l)} \\ kp_g = \rho_g\omega v + \dfrac{\rho_g}{\phi S^g}\omega w^{(g)} - \dfrac{i\mu_g}{\kappa_r^g\kappa}w^{(g)} \\ \omega\sigma = k\big[-(\lambda+2\mu+\alpha\gamma a_{11}+\alpha(1-\gamma)a_{21})v \\ \qquad - w^{(l)}\alpha(\gamma a_{12}+(1-\gamma)a_{22}) - w^{(g)}\alpha(\gamma a_{13} \\ \quad +(1-\gamma)a_{23})\big] \\ \quad +\omega T(1+i\tau_1\omega(1-\epsilon))(\alpha\gamma a_{14} \\ \quad +\alpha(1-\gamma)a_{24}-\beta_s) \\ \omega p_l = k\big[a_{11}v + a_{12}w^{(l)} + a_{13}w^{(g)}\big] \\ \quad - a_{14}\omega T[1+i\omega\tau_1(1-\epsilon)] \\ \omega p_g = k\big[a_{21}v + a_{22}w^{(l)} + a_{23}w^{(g)}\big] \\ \quad - a_{24}\omega T[1+i\omega\tau_1(1-\epsilon)] \\ d_2kv(\epsilon\tau_q\omega - i) + d_3kw^{(l)}(\epsilon\tau_q\omega - i) + d_4kw^{(g)}(\epsilon\tau_q\omega - i) \\ \quad = T\left(e_1\omega^2 - e_2 i\omega - Kk^2\right) \end{cases} \tag{B.2}$$

where

$$e_1 = c\tau_q + d_1(1-\epsilon)\tau_1 + d_1\epsilon\tau_q, \qquad e_2 = c + d_1. \tag{B.3}$$

The above equations constitute a homogeneous system of linear equations whose solution is not 0 if the determinant of matrix **B** is 0, whose components are

$$\begin{aligned} &b_{11} = \rho v_c, b_{12} = \rho_l v_c, b_{13} = \rho_g v_c, b_{14} = 1 \\ &b_{15} = b_{16} = b_{17} = 0 \\ &b_{21} = \rho_l v_c, b_{22} = H_1 v_c, b_{23} = b_{24} = 0, b_{25} = -1 \\ &b_{26} = b_{27} = 0 \\ &b_{31} = \rho_g v_c, b_{32} = 0, b_{33} = H_2 v_c, b_{34} = b_{35} = 0 \\ &b_{36} = -1, b_{37} = 0 \\ &b_{41} = -D_1, \quad b_{42} = -D_2, \quad b_{43} = -D_3, \quad b_{44} = -v_c \\ &b_{45} = b_{46} = 0, b_{47} = D_4 v_c G_1 \\ &b_{51} = a_{11}, \quad b_{52} = a_{12}, \quad b_{53} = a_{13}, \quad b_{54} = 0 \\ &b_{55} = -v_c, \quad b_{56} = 0, \quad b_{57} = -a_{14}v_c G_1 \\ &b_{61} = a_{21}, \quad b_{62} = a_{22}, \quad b_{63} = a_{23}, \quad b_{64} = 0 \\ &b_{65} = 0, b_{66} = -v_c, \quad b_{67} = -a_{24}v_c G_1 \\ &b_{71} = d_2 G_2 v_c, \quad b_{72} = d_3 G_2 v_c, \quad b_{73} = d_4 G_2 v_c \\ &b_{74} = 0, \quad b_{75} = 0, \quad b_{76} = 0, b_{77} = K - v_c^2 G_3 \end{aligned} \tag{B.4}$$

where

$$\begin{aligned} &G_1 = 1 + i\omega\tau_1(1-\epsilon),\ G_2 = \epsilon\tau_q - i/\omega,\ G_3 = e_1 - ie_2/\omega \\ &H_1 = \frac{\rho_l}{\phi S^l} - \frac{ib_l}{\omega},\ H_2 = \frac{\rho_g}{\phi S^g} - \frac{ib_g}{\omega} \\ &D_1 = \lambda + 2\mu + \alpha\gamma a_{11} + \alpha(1-\gamma)a_{21} \\ &D_2 = \alpha\gamma a_{12} + \alpha(1-\gamma)a_{22},\ D_3 = \alpha\gamma a_{13} + \alpha(1-\gamma)a_{23} \\ &D_4 = \alpha\gamma a_{14} + \alpha(1-\gamma)a_{24} - \beta_s. \end{aligned} \tag{B.5}$$

Based on the above equations, we obtain the dispersion relation for P waves as

$$a_8 v_c^8 + a_6 v_c^6 + a_4 v_c^4 + a_2 v_c^2 + a_0 = 0 \tag{B.6}$$

where the coefficients a_8, a_6, a_4, a_2, and a_0 are given in (B.7), as shown at the bottom of the page.

Solving (B.6), we obtain four physically meaningful roots, three of which are complex velocities of the compressional waves (P), denoted as P1, P2 and P3 waves. The fourth one corresponds to the velocity of the thermal wave. In particular, by setting β_T, β_ψ, β_{sT}, β_{wT}, and p_g^* to zero, we obtain a decoupled thermal velocity

$$v_c = \sqrt{\frac{i\omega a^2}{1 + i\omega\tau_q}} \tag{B.8}$$

$$\begin{aligned} a_8 = {} & G_3(\rho H_1 H_2 - H_1\rho_g^2 - H_2\rho_l^2) \\ a_6 = {} & K(H_1\rho_g^2 + H_2\rho_l^2 - \rho H_1 H_2) + G_3(a_{12}\rho_g^2 + a_{23}\rho_l^2 - (a_{13}+a_{22})\rho_g\rho_l) + G_3 H_1(-D_1 H_2 + D_3\rho_g - a_{23}\rho + a_{21}\rho_g) \\ & + G_3 H_2(D_2\rho_l - a_{12}\rho + a_{11}\rho_l) + G_1 G_2\big[-a_{14}d_3\rho_g^2 - a_{24}d_4\rho_l^2 + (a_{14}d_4 + a_{24}d_3)\rho_g\rho_l - \rho_g(D_4 H_1 d_4 + H_1 a_{24} d_2) \\ & - \rho_l(D_4 H_2 d_3 + H_2 a_{14} d_2) + \rho(H_2 a_{14} d_3 + H_1 a_{24} d_4) + D_4 H_1 H_2 d_2\big] \\ a_4 = {} & K(a_{13}\rho_g\rho_l + a_{22}\rho_g\rho_l - a_{12}\rho_g^2 - a_{23}\rho_l^2 + H_2 a_{12}\rho + H_1 a_{23}\rho - H_2 a_{11}\rho_l - H_1 a_{21}\rho_g + D_1 H_1 H_2 - D_3 H_1\rho_g - D_2 H_2\rho_l) \\ & + G_3\big[H_2(D_1 a_{12} - D_2 a_{11}) + \rho(a_{12}a_{23} - a_{13}a_{22}) + \rho_g(D_2 a_{13} - D_3 a_{12} + a_{11}a_{22} - a_{12}a_{21}) \\ & + \rho_l(D_3 a_{22} - D_2 a_{23} + a_{13}a_{21} - a_{11}a_{23}) + H_1(D_1 a_{23} - D_3 a_{21})\big] \\ & - G_1 G_2 D_1(H_2 a_{14} d_3 + H_1 a_{24} d_4) + G_1 G_2 D_2(H_2 a_{14} d_2 - a_{14} d_4\rho_g + a_{24} d_4\rho_l) + G_1 G_2 D_3(H_1 a_{24} d_2 + a_{14} d_3\rho_g - a_{24} d_3\rho_l) \\ & + G_1 G_2 D_4(H_2 a_{11} d_3 - H_2 a_{12} d_2 + H_1 a_{21} d_4 - H_1 a_{23} d_2 + a_{12} d_4\rho_g - a_{13} d_3\rho_g - a_{22} d_4\rho_l + a_{23} d_3\rho_l) \\ & + G_1 G_2\rho(a_{13}a_{24}d_3 - a_{12}a_{24}d_4 + a_{14}a_{22}d_4 - a_{14}a_{23}d_3) + G_1 G_2\rho_g(a_{12}a_{24}d_2 - a_{11}a_{24}d_3 + a_{14}a_{21}d_3 - a_{14}a_{22}d_2) \\ & + G_1 G_2\rho_l(a_{11}a_{24}d_4 - a_{13}a_{24}d_2 + a_{14}a_{23}d_2 - a_{14}a_{21}d_4) \\ a_2 = {} & K(D_2 H_2 a_{11} - D_1 H_2 a_{12} - D_1 H_1 a_{23} + D_3 H_1 a_{21} - D_2 a_{13}\rho_g + D_3 a_{12}\rho_g + D_2 a_{23}\rho_l - D_3 a_{22}\rho_l - a_{12}a_{23}\rho + a_{13}a_{22}\rho \\ & - a_{11}a_{22}\rho_g + a_{12}a_{21}\rho_g + a_{11}a_{23}\rho_l - a_{13}a_{21}\rho_l) + G_3\big[D_1(a_{13}a_{22} - a_{12}a_{23}) + D_2(a_{11}a_{23} - a_{13}a_{21}) + D_3(a_{12}a_{21} - a_{11}a_{22})\big] \\ & + G_1 G_2 D_1(a_{12}a_{24}d_4 - a_{13}a_{24}d_3 - a_{14}a_{22}d_4 + a_{14}a_{23}d_3) + G_1 G_2 D_2(a_{13}a_{24}d_2 - a_{11}a_{24}d_4 - a_{14}a_{23}d_2 + a_{14}a_{21}d_4) \\ & + G_1 G_2 D_3(a_{11}a_{24}d_3 - a_{12}a_{24}d_2 - a_{14}a_{21}d_3 + a_{14}a_{22}d_2) \\ & + G_1 G_2 D_4(a_{11}a_{22}d_4 - a_{11}a_{23}d_3 - a_{12}a_{21}d_4 + a_{12}a_{23}d_2 + a_{13}a_{21}d_3 - a_{13}a_{22}d_2) \\ a_0 = {} & K[D_1(a_{12}a_{23} - a_{13}a_{22}) + D_2(a_{13}a_{21} - a_{11}a_{23}) + D_3(a_{11}a_{22} - a_{12}a_{21})] \end{aligned} \tag{B.7}$$

where $a = \sqrt{K/c}$ is the thermal diffusivity [25]. At low frequencies, this velocity is zero. The dispersion relation corresponding to the fast and slow acoustic waves becomes a cubic one

$$c_6 v_c^6 + c_4 v_c^4 + c_2 v_c^2 + c_0 = 0 \tag{B.9}$$

where

$$\begin{aligned}
c_6 &= H_1\rho_g^2 + H_2\rho_l^2 - H_1H_2\rho \\
c_4 &= -a_{12}\rho_g^2 - a_{23}\rho_l^2 + D_1H_1H_2 - D_3H_1\rho_g - D_2H_2\rho_l \\
&\quad + H_2a_{12}\rho + H_1a_{23}\rho - H_2a_{11}\rho_l - H_1a_{21}\rho_g + a_{13}\rho_g\rho_l \\
&\quad + a_{22}\rho_g\rho_l \\
c_2 &= -D_1H_2a_{12} + D_2H_2a_{11} - D_1H_1a_{23} + D_3H_1a_{21} \\
&\quad - D_2a_{13}\rho_g + D_3a_{12}\rho_g + D_2a_{23}\rho_l - D_3a_{22}\rho_l - a_{12}a_{23}\rho \\
&\quad + a_{13}a_{22}\rho - a_{11}a_{22}\rho_g + a_{12}a_{21}\rho_g + a_{11}a_{23}\rho_l - a_{13}a_{21}\rho_l \\
c_0 &= D_1a_{12}a_{23} - D_1a_{13}a_{22} - D_2a_{11}a_{23} + D_2a_{13}a_{21} \\
&\quad + D_3a_{11}a_{22} - D_3a_{12}a_{21}.
\end{aligned} \tag{B.10}$$

The phase velocity and the attenuation factor can be obtained from the complex velocity v_c as

$$v_p = [\mathrm{Re}(v_c^{-1})]^{-1}, \quad Q = \mathrm{Re}(v_c^2)/\mathrm{Im}(v_c^2) \tag{B.11}$$

where "Re" and "Im" take the real and imaginary parts of a complex variable, respectively [36].

Appendix C
Crank–Nicolson Explicit Scheme

The Crank–Nicolson scheme has been applied by Carcione *et al.* [25], [26] to solve the thermoelasticity and thermo-poroelasticity equations. This scheme, adapted to the present case, is

$$\begin{aligned}
D^{1/2}v_x &= \beta_{11}(\sigma_{xx,x} + \sigma_{xz,z} - f_x)^n - \beta_{12}p_{l,x}^n \\
&\quad - \beta_{12}b_lA^{1/2}w_x^{(l)} - \beta_{13}p_{g,x}^n - \beta_{13}b_gA^{1/2}w_x^{(g)} = \mathrm{II}_x^n \\
D^{1/2}v_z &= \beta_{11}(\sigma_{xz,x} + \sigma_{zz,z} - f_z)^n - \beta_{12}p_{l,z}^n \\
&\quad - \beta_{12}b_lA^{1/2}w_z^{(l)} - \beta_{13}p_{g,z}^n - \beta_{13}b_gA^{1/2}w_z^{(g)} = \mathrm{II}_z^n \\
D^{1/2}w_x^{(l)} &= \beta_{21}(\sigma_{xx,x} + \sigma_{xz,z} - f_x)^n - \beta_{22}p_{l,x}^n \\
&\quad - \beta_{22}b_lA^{1/2}w_x^{(l)} - \beta_{23}p_{g,x}^n - \beta_{23}b_gA^{1/2}w_x^{(g)} = \Omega_x^n \\
D^{1/2}w_z^{(l)} &= \beta_{21}(\sigma_{xz,x} + \sigma_{zz,z} - f_z)^n - \beta_{22}p_{l,z}^n \\
&\quad - \beta_{22}b_lA^{1/2}w_z^{(l)} - \beta_{23}p_{g,z}^n - \beta_{23}b_gA^{1/2}w_z^{(g)} = \Omega_z^n \\
D^{1/2}w_x^{(g)} &= \beta_{31}(\sigma_{xx,x} + \sigma_{xz,z} - f_x)^n - \beta_{32}p_{l,x}^n \\
&\quad - \beta_{32}b_lA^{1/2}w_x^{(l)} - \beta_{33}p_{g,x}^n - \beta_{33}b_gA^{1/2}w_x^{(g)} = \Gamma_x^n \\
D^{1/2}w_z^{(g)} &= \beta_{31}(\sigma_{xz,x} + \sigma_{zz,z} - f_z)^n - \beta_{32}p_{l,z}^n \\
&\quad - \beta_{32}b_lA^{1/2}w_z^{(l)} - \beta_{33}p_{g,z}^n - \beta_{33}b_gA^{1/2}w_z^{(g)} = \Gamma_z^n \\
\epsilon_m &= (A^{1/2}v_x)_{,x} + (A^{1/2}v_z)_{,z} \\
\dot{\epsilon}_m &= \left(\mathrm{II}_x^n\right)_{,x} + \left(\mathrm{II}_z^n\right)_{,z} \\
\epsilon_l &= \left(A^{1/2}w_x^{(l)}\right)_{,x} + \left(A^{1/2}w_z^{(l)}\right)_{,z} \\
\dot{\epsilon}_l &= \left(\Omega_x^n\right)_{,x} + \left(\Omega_z^n\right)_{,z} \\
\epsilon_g &= \left(A^{1/2}w_x^{(g)}\right)_{,x} + \left(A^{1/2}w_z^{(g)}\right)_{,z} \\
\dot{\epsilon}_g &= \left(\Gamma_x^n\right)_{,x} + \left(\Gamma_z^n\right)_{,z} \\
K\nabla^2T^n &= e_2A^{1/2}\psi + e_1D^{1/2}\psi + d_2[\epsilon_m + \epsilon\tau_q\dot{\epsilon}_m] \\
&\quad + d_3[\epsilon_l + \epsilon\tau_q\dot{\epsilon}_l] + d_4[\epsilon_g + \epsilon\tau_q\dot{\epsilon}_g] + q^n \\
T^{n+1} &= T^n + dt\,\psi^{n+1/2} \\
D^1\sigma_{xx} &= 2\mu(A^{1/2}v_x)_{,x} + [D_1 - 2\mu]\epsilon_m + D_2\epsilon_l + D_3\epsilon_g \\
&\quad + D_4A^{1/2}\psi + D_4(1-\epsilon)\tau_1D^{1/2}\psi + f_{xx}^n \\
D^1\sigma_{zz} &= 2\mu(A^{1/2}v_z)_{,z} + [D_1 - 2\mu]\epsilon_m + D_2\epsilon_l + D_3\epsilon_g \\
&\quad + D_4A^{1/2}\psi + D_4(1-\epsilon)\tau_1D^{1/2}\psi + f_{zz}^n \\
D^1\sigma_{xz} &= \mu[(A^{1/2}v_x)_{,z} + (A^{1/2}v_z)_{,x}] + f_{xz}^n \\
D^1p_l &= -a_{11}\epsilon_m - a_{12}\epsilon_l - a_{13}\epsilon_g \\
&\quad - a_{14}A^{1/2}\psi - a_{14}(1-\epsilon)\tau_1D^{1/2}\psi - f_l^n \\
D^1p_g &= -a_{21}\epsilon_m - a_{22}\epsilon_l - a_{23}\epsilon_g \\
&\quad - a_{24}A^{1/2}\psi - a_{24}(1-\epsilon)\tau_1D^{1/2}\psi - f_g^n
\end{aligned} \tag{C.1}$$

where

$$D^j\phi = \frac{\phi^{n+j} - \phi^{n-j}}{2j\,dt}, \quad A^j\phi = \frac{\phi^{n+j} + \phi^{n-j}}{2} \tag{C.2}$$

are the central differences and mean value operators. In this scheme, the particle velocities and ψ at time $(n+1/2)dt$, and stresses and T at time $(n+1)dt$ are computed from particle velocities and ψ at time $(n-1/2)dt$ and stresses and T at time ndt and $(n-1)dt$, respectively.

For example, by using (C.1), in the absence of sources, $w_x^{(l)}$ and $w_x^{(g)}$ can be updated as

$$\begin{aligned}
&\begin{bmatrix} 1+a_{11} & a_{12} \\ a_{21} & 1+a_{22} \end{bmatrix}\begin{bmatrix} w_x^{(l)^{n+1/2}} \\ w_x^{(g)^{n+1/2}} \end{bmatrix} \\
&\quad = \begin{bmatrix} 1-a_{11} & -a_{12} \\ -a_{21} & 1-a_{22} \end{bmatrix}\begin{bmatrix} w_x^{(l)^{n-1/2}} \\ w_x^{(g)^{n-1/2}} \end{bmatrix} \\
&\qquad + dt\begin{bmatrix} \beta_{21}(\sigma_{xx,x} + \sigma_{xz,z})^n - \beta_{22}p_{l,x}^n - \beta_{23}p_{g,x}^n \\ \beta_{31}(\sigma_{xx,x} + \sigma_{xz,z})^n - \beta_{32}p_{l,x}^n - \beta_{33}p_{g,x}^n \end{bmatrix}
\end{aligned} \tag{C.3}$$

where $a_{11} = dt\beta_{22}b_l/2$, $a_{12} = \beta_{23}b_g dt/2$, $a_{21} = dt\beta_{32}b_l/2$, and $a_{22} = \beta_{33}b_g dt/2$.

Then,

$$\begin{aligned}
2v_x^{n+1/2} &= 2v_x^{n-1/2} + 2dt\beta_{11}(\sigma_{xx,x} + \sigma_{xz,z})^n \\
&\quad - 2dt\left[\beta_{12}p_{l,x}^n + \beta_{13}p_{g,x}^n\right] \\
&\quad - dt\beta_{12}b_l\left(w_x^{(l)^{n+1/2}} + w_x^{(l)^{n-1/2}}\right) \\
&\quad - dt\beta_{13}b_g\left(w_x^{(g)^{n+1/2}} + w_x^{(g)^{n-1/2}}\right).
\end{aligned} \tag{C.4}$$

The other particle velocities can be similarly updated, which are then used to obtain the updated ϵ_i and $\dot{\epsilon}_i$, $i = m, l, g$, following (C.1).

A further simplification of the temperature equation for ψ is

$$\begin{aligned}
(dte_2 + 2e_1)\psi^{n+1/2} &= -(dte_2 - 2e_1)\psi^{n-1/2} \\
&\quad + 2dt[K\nabla^2T^n - d_2(\epsilon_m + \epsilon\tau_q\dot{\epsilon}_m) \\
&\quad - d_3(\epsilon_l + \epsilon\tau_q\dot{\epsilon}_l) - d_4(\epsilon_g + \epsilon\tau_q\dot{\epsilon}_g)].
\end{aligned} \tag{C.5}$$

The stress σ_{xx} is calculated as

$$\begin{aligned}
\sigma_{xx}^{n+1} &= \sigma_{xx}^{n-1} + 2dt\left[2\mu(A^{1/2}v_x)_{,x} + [D_1 - 2\mu]\epsilon_m \right. \\
&\quad \left. + D_2\epsilon_l + D_3\epsilon_g + D_4A^{1/2}\psi + D_4(1-\epsilon)\tau_1D^{1/2}\psi\right].
\end{aligned} \tag{C.6}$$

The equations for the other stresses can be similarly obtained.

TABLE II
CRANK–NICOLSON SCHEME

Input:

The initialized wavefields, σ_{xx}^{-1}, σ_{xx}^{0}, σ_{zz}^{-1}, σ_{zz}^{0}, σ_{xz}^{-1}, σ_{xz}^{0}, p_l^{-1}, p_l^{0}, p_g^{-1}, p_g^{0}, ${w_x^{(l)}}^{-1/2}$, ${w_z^{(l)}}^{-1/2}$, ${w_x^{(g)}}^{-1/2}$, ${w_z^{(g)}}^{-1/2}$, $v_x^{-1/2}$, $v_z^{-1/2}$, $\psi^{-1/2}$, T^0;

Receiver location (Rx, Rz).

Output:

Simulated wavefields at time ndt: ${w_x^{(l)}}^{n+1/2}$, ${w_z^{(l)}}^{n+1/2}$, ${w_x^{(g)}}^{n+1/2}$, ${w_z^{(g)}}^{n+1/2}$, $v_x^{n+1/2}$, $v_z^{n+1/2}$, T^{n+1};

Waveforms of particle velocities and T at Receiver location (Rx, Rz).

1: **for** $t = 0$; $t \le N$; t++ **do**
2: // update particle velocities with stresses at time t.
Update ${w_x^{(l)}}^{t+1/2}$, ${w_x^{(g)}}^{t+1/2}$ and $v_x^{t+1/2}$ using (C.3) and (C.4);
Update ${w_z^{(l)}}^{t+1/2}$, ${w_z^{(g)}}^{t+1/2}$ and $v_z^{t+1/2}$, similarly;
Output particle velocities, if $t = n$;
3: // update ψ with particle velocities at $t \pm 1/2$.
Update ϵ_m, ϵ_l, ϵ_g, $\dot{\epsilon}_m$, $\dot{\epsilon}_l$ and $\dot{\epsilon}_g$ using (C.1);
Update $\psi^{t+1/2}$, based on equation (C.5);
4: // update T.
T^{t+1}=T^t+$dt\psi^{t+1/2}$;
Output T^{n+1}, if $t = n$;
5: // update stresses with particle velocities and ψ at $t \pm 1/2$.
Update σ_{xx}^{t+1} using equation (C.6);
Update σ_{zz}^{t+1}, σ_{xz}^{t+1}, p_l^{t+1} and p_g^{t+1}, similarly;
6: **end for**
7: return waveforms of the v_x, v_z, $w_x^{(l)}$, $w_z^{(l)}$, $w_x^{(g)}$, $w_z^{(g)}$ and T at location (Rx, Rz) for all $t = 0 : N$.

As stated in [26], the temporal Crank–Nicolson scheme is first-order accurate, which has the stability properties of implicit algorithms, but the solution can be obtained explicitly, which overcomes the stiff and instability problems effectively.

We solve the spatial derivatives in (C.1) by using the optimized staggered-grid FD scheme [29], to better control the dispersion. Specifically, the first-order derivative of a function $p(x)$ can be calculated as

$$\frac{\partial p}{\partial x} = \frac{1}{h}\sum_{m=1}^{M} c_m[p(x+mh-0.5h) - p(x-mh+0.5h)] \tag{C.7}$$

where x is the location, h is the spatial spacing, and c_m are the FD coefficients, which can be determined by minimizing the absolute dispersion error over a wavenumber interval $[0, b]$ using the least-square method

$$\sum_{m=2}^{M}\left[\int_0^b \psi_m(\beta)\psi_n(\beta)\mathrm{d}\beta\right]c_m = \int_0^b g(\beta)\psi_n(\beta)\mathrm{d}\beta \tag{C.8}$$

for $n = 2, 3, \ldots, M$, where

$$\begin{aligned}\psi_k(\beta) &= 2\sin[(k-0.5)\beta] - 4(k-0.5)\sin(0.5\beta)\\ g(\beta) &= \beta - 2\sin(0.5\beta)\end{aligned} \tag{C.9}$$

and

$$c_1 = 1 - \sum_{m=2}^{M}(2m-1)c_m. \tag{C.10}$$

It is suggested in [29] that the optimized FD method can have a wider wavenumber range than the traditional Taylor-expansion-based method. We determine the value of b for the given M so that the maximum dispersion error is $\eta = 10^{-5}$.

In Table II, we illustrate the Crank–Nicolson algorithm in pseudocode form.

ACKNOWLEDGMENT

The authors would like to thank the Editor, Simon H. Yueh, the Associate Editor, M. D. Sacchi, and three anonymous reviewers for their constructive comments and suggestions.

REFERENCES

[1] M. A. Biot, "Theory of propagation of elastic waves in a fluid-saturated porous solid. I. Low-frequency range," *J. Acoust. Soc. Amer.*, vol. 28, no. 2, pp. 168–178, Mar. 1956.

[2] M. A. Biot, "Thermoelasticity and irreversible thermodynamics," *J. Appl. Phys.*, vol. 27, no. 3, pp. 240–253, Mar. 1956.

[3] H. Deresiewicz, "Plane waves in a thermoelastic solid," *J. Acoust. Soc. Amer.*, vol. 29, no. 2, pp. 204–209, 1957.

[4] J. N. Sharma, V. Kumar, and D. Chand, "Reflection of generalized thermoelastic waves from the boundary of a half-space," *J. Thermal Stresses*, vol. 26, no. 10, pp. 925–942, Oct. 2003.

[5] M. D. Sharma, "Wave propagation in thermoelastic saturated porous medium," *J. Earth Syst. Sci.*, vol. 117, no. 6, pp. 951–958, Dec. 2008.

[6] W. Wei, R. Zheng, G. Liu, and H. Tao, "Reflection and refraction of p wave at the interface between thermoelastic and porous thermoelastic medium," *Transp. Porous Media*, vol. 113, no. 1, pp. 1–27, May 2016.

[7] M. A. Biot, "Mechanics of deformation and acoustic propagation in porous media," *J. Appl. Phys.*, vol. 33, no. 4, pp. 1482–1498, Apr. 1962.

[8] Y. Qing Zeng and Q. Huo Liu, "Acoustic detection of buried objects in 3-D fluid saturated porous media: Numerical modeling," *IEEE Trans. Geosci. Remote Sens.*, vol. 39, no. 6, pp. 1165–1173, Jun. 2001.

[9] Y. Zhang, J. Gao, and J. Peng, "Variable-order finite difference scheme for numerical simulation in 3-D poroelastic media," *IEEE Trans. Geosci. Remote Sens.*, vol. 56, no. 5, pp. 2991–3001, May 2018.

[10] Q. Zhan, M. Zhuang, and Q. H. Liu, "A compact upwind flux with more physical insight for wave propagation in 3-D poroelastic media," *IEEE Trans. Geosci. Remote Sens.*, vol. 56, no. 10, pp. 5794–5801, Oct. 2018.

[11] Q. Zhan, M. Zhuang, Z. Zhou, J.-G. Liu, and Q. H. Liu, "Complete-Q model for poro-viscoelastic media in subsurface sensing: Large-scale simulation with an adaptive DG algorithm," *IEEE Trans. Geosci. Remote Sens.*, vol. 57, no. 7, pp. 4591–4599, Jul. 2019.

[12] J. E. Santos, J. Douglas, Jr, J. Corberó, and O. M. Lovera, "A model for wave propagation in a porous medium saturated by a two-phase fluid," *J. Acoust. Soc. Amer.*, vol. 87, no. 4, pp. 1439–1448, 1990.

[13] W.-C. Lo, G. Sposito, and E. Majer, "Wave propagation through elastic porous media containing two immiscible fluids," *Water Resour. Res.*, vol. 41, no. 2, Feb. 2005, Art. no. W02025.

[14] J. M. Carcione and G. Seriani, "Wave simulation in frozen porous media," *J. Comput. Phys.*, vol. 170, no. 2, pp. 676–695, Jul. 2001.

[15] J. M. Carcione, J. E. Santos, C. L. Ravazzoli, and H. B. Helle, "Wave simulation in partially frozen porous media with fractal freezing conditions," *J. Appl. Phys.*, vol. 94, no. 12, pp. 7839–7847, 2003.

[16] J. E. Santos, C. L. Ravazzoli, and J. M. Carcione, "A model for wave propagation in a composite solid matrix saturated by a single-phase fluid," *J. Acoust. Soc. Amer.*, vol. 115, no. 6, pp. 2749–2760, Jun. 2004.

[17] S. R. Pride, J. G. Berryman, and J. M. Harris, "Seismic attenuation due to wave-induced flow," *J. Geophys. Res., Solid Earth*, vol. 109, no. B1, Jan. 2004, Art. no. B01201.

[18] J. Ba, J. M. Carcione, and J. X. Nie, "Biot-Rayleigh theory of wave propagation in double-porosity media," *J. Geophys. Res.*, vol. 116, no. B6, 2011, Art. no. B06202.

[19] J. E. Santos, C. L. Ravazzoli, P. M. Gauzellino, J. M. Carcione, and F. Cavallini, "Simulation of waves in poro-viscoelastic rocks saturated by immiscible fluids: Numerical evidence of a second slow wave," *J. Comput. Acoust.*, vol. 12, no. 1, pp. 1–21, Mar. 2004.

[20] J. M. Carcione, F. Cavallini, J. E. Santos, C. L. Ravazzoli, and P. M. Gauzellino, "Wave propagation in partially saturated porous media: Simulation of a second slow wave," *Wave Motion*, vol. 39, no. 3, pp. 227–240, 2004.

[21] J. M. Carcione, D. Gei, J. E. Santos, L.-Y. Fu, and J. Ba, "Canonical analytical solutions of wave-induced thermoelastic attenuation," *Geophys. J. Int.*, vol. 221, no. 2, pp. 835–842, May 2020.

[22] H. W. Lord and Y. Shulman, "A generalized dynamical theory of thermoelasticity," *J. Mech. Phys. Solids*, vol. 15, no. 5, pp. 299–309, Sep. 1967.

[23] A. E. Green and K. A. Lindsay, "Thermoelasticity," *J. Elasticity*, vol. 2, no. 1, pp. 1–7, 1972.

[24] A. J. Rudgers, "Analysis of thermoacoustic wave propagation in elastic media," *J. Acoust. Soc. Amer.*, vol. 88, no. 2, pp. 1078–1094, Aug. 1990.

[25] J. M. Carcione, Z.-W. Wang, W. Ling, E. Salusti, J. Ba, and L.-Y. Fu, "Simulation of wave propagation in linear thermoelastic media," *Geophysics*, vol. 84, no. 1, pp. T1–T11, Jan. 2019.

[26] J. M. Carcione, F. Cavallini, E. Wang, J. Ba, and L. Fu, "Physics and simulation of wave propagation in linear thermoporoelastic media," *J. Geophys. Res., Solid Earth*, vol. 124, no. 8, pp. 8147–8166, Aug. 2019.

[27] K. Shukla, J. M. Carcione, P. Jaiswal, J. E. Santos, and J. Ba, "Effect of capillary pressure on seismic velocities and attenuation," *J. Porous Media*, vol. 22, no. 4, pp. 447–466, 2019.

[28] F. Zhou, H. Liu, and S. Li, "Propagation of thermoelastic waves in unsaturated porothermoelastic media," *J. Thermal Stresses*, vol. 42, no. 10, pp. 1256–1271, 2019.

[29] Y. Liu, "Optimal staggered-grid finite-difference schemes based on least-squares for wave equation modelling," *Geophys. J. Int.*, vol. 197, no. 2, pp. 1033–1047, 2014.

[30] J. Ignaczak and M. Ostoja-Starzewski, *Thermoelasticity With Finite Wave Speeds*. Oxford, U.K.: OUP Oxford, 2010.

[31] T. M. Müller, B. Gurevich, and M. Lebedev, "Seismic wave attenuation and dispersion resulting from wave-induced flow in porous rocksła review," *Geophysics*, vol. 75, no. 5, 2010, Art. no. 75A147.

[32] T. McNelly *et al.*, "Heat pulses in naf: Onset of second sound," *Phys. Rev. Lett.*, vol. 24, no. 3, p. 100, 1970.

[33] S. Huberman *et al.*, "Observation of second sound in graphite at temperatures above 100 k," *Science*, vol. 364, no. 6438, pp. 375–379, Apr. 2019.

[34] A. A. Abed and W. T. Sołowski, "A study on how to couple thermo-hydro-mechanical behaviour of unsaturated soils: Physical equations, numerical implementation and examples," *Comput. Geotechnics*, vol. 92, pp. 132–155, Dec. 2017.

[35] M. T. van Genuchten, "A closed-form equation for predicting the hydraulic conductivity of unsaturated soils," *Soil Sci. Soc. Amer. J.*, vol. 44, no. 5, pp. 892–898, Sep. 1980.

[36] J. M. Carcione, *Wave Fields in Real Media. Theory and Numerical Simulation of Wave Propagation in Anisotropic, Anelastic, Porous and Electromagnetic Media*. Amsterdam, The Netherlands: Elsevier, 2014.

Enjiang Wang received the B.S. degree in geophysics from China University of Petroleum, Qingdao, China, in 2012, and the Ph.D. degree in exploration geophysics from the China University of Petroleum, Beijing, China, in 2017.

He is an Assistant Professor with the College of Marine Geosciences, Ocean University of China, Qingdao. His research interests include seismic rock physics, wavefield modeling, and seismic imaging.

José M. Carcione received the Licenciado in Ciencias Físicas degree from the University of Buenos Aires, Buenos Aires, Argentina, in 1978, the Dottore in Fisica degree from the University of Milan, Milan, Italy, in 1984, and the Ph.D. degree in geophysics from Tel Aviv University, Tel Aviv, Israel, in 1987.

He is a Senior Geophysicist with the National Institute of Oceanography and Applied Geophysics (OGS), Trieste, Italy. His research interests include numerical modeling, the theory of wave propagation in acoustic and electromagnetic media, and their application to geophysics.

Jing Ba received the B.S. degree in geophysics from Yunnan University, Kunming, China, in 2001, the M.S. degree in geophysics from the Institute of Geology, China Earthquake Administration, Beijing, China, in 2004, and the Ph.D. degree in mechanics from Tsinghua University, Beijing, in 2008.

He is a Professor with Hohai University, Nanjing, China. His research interests include rock physics theory, seismic forward modeling, and reservoir identification.